

## Layer-by-Layer Electrodeposited Reduced Graphene Oxide-Copper Nanopolyhedra Films as Efficient Platinum-Free Counter Electrodes in High Efficiency Dye-Sensitized Solar Cells

To cite this article: M. Sookhakian *et al* 2016 *J. Electrochem. Soc.* **163** D154

View the [article online](#) for updates and enhancements.

### You may also like

- [Chemically-reduced graphene reinforced polyetherimide nanocomposites: dielectric behavior, thermal stability and mechanical properties](#)  
Md Wasi Ahmad, Baban Dey, Anood ALMezeni *et al.*
- [Fabrication of poly \(trimethylene carbonate\)/reduced graphene oxide-graft-poly \(trimethylene carbonate\) composite scaffolds for nerve regeneration](#)  
Zhengchao Guo, Jia Liang, Marc J K Ankone *et al.*
- [Cobalt ferrite nanoparticles supported on reduced graphene oxide sheets: optical, magnetic and magneto-antibacterial studies](#)  
Alireza Meidanchi



245th ECS Meeting • May 26-30, 2024 • San Francisco, CA

Present your work at the leading electrochemistry & solid-state science conference.

Network with academic, government, and industry influencers!

Submit abstracts by December 1, 2023

[Learn more & submit!](#)





# Layer-by-Layer Electrodeposited Reduced Graphene Oxide-Copper Nanopolyhedra Films as Efficient Platinum-Free Counter Electrodes in High Efficiency Dye-Sensitized Solar Cells

M. Sookhakian,<sup>a,b,z</sup> N. A. Ridwan,<sup>a</sup> E. Zalnezhad,<sup>b,z</sup> G. H. Yoon,<sup>b</sup> Majid Azarang,<sup>c</sup> M. R. Mahmoudian,<sup>a</sup> and Y. Alias<sup>a,z</sup>

<sup>a</sup>Department of Chemistry, Faculty of Science, University of Malaya, Kuala Lumpur 50603, Malaysia

<sup>b</sup>Department of Mechanical Convergence Engineering, Hanyang University, 222 Wangsimni-ro, Seongdong-gu, Seoul 133-791, Korea

<sup>c</sup>Department of Physics, Faculty of Science, University of Malaya, Kuala Lumpur 50603, Malaysia

Efficient and low-cost platinum-free counter electrodes consisting of reduced graphene oxide (rGO) and copper nanopolyhedra (Cu) were fabricated on indium tin oxide (ITO) glass using a layer-by-layer electrochemical deposition. The structure and morphology of the as-fabricated counter electrodes were confirmed by X-ray diffraction, field-emission electron microscopy, and Raman spectroscopy. rGO-Cu-modified ITO electrodes, with different rGO loadings, were applied as catalytic counter electrodes in dye-sensitized solar cells (DSSCs) with an electrodeposited ZnO nanorod array as the photoanode. The current density–voltage curves and transient photocurrent measurements illustrate that the power conversion efficiency of the ZnO nanorod photoanode is significantly improved by the formation of rGO on the counter electrode. On the basis of electrochemical impedance spectroscopy, it is determined that the increased electrocatalytic activity of the rGO-Cu counter electrode is due to an enhanced conductivity of the counter electrodes. The maximum conversion efficiency is obtained for the rGO-Cu counter electrode with 0.5 mg ml<sup>−1</sup> of rGO and has one and one half the efficiency achieved using a counter electrode modified only with Cu nanopolyhedra.

© 2016 The Electrochemical Society. [DOI: 10.1149/2.0561605jes] All rights reserved.

Manuscript submitted December 8, 2015; revised manuscript received January 15, 2016. Published January 29, 2016.

The shortage of fossil fuels and the continuing rise in the population are creating a higher demand for new energy resources. Therefore, research is being performed to find alternative energy resources that are inexpensive, non-toxic and environmentally friendly. Solar energy, as the cleanest and least limited source of energy, is considered to be an alternative to conventional fossil fuels. Currently, the vast majority of commercial solar cell modules are based on crystalline silicon because of its high efficiency (approximately 24%). However, this high efficiency is offset by the high cost of commercial solar cell modules.<sup>1</sup> To overcome this challenge, many efforts have been focused on developing photovoltaic devices that are inexpensive but possess high stabilities and efficiencies.<sup>2</sup> Dye-sensitized solar cells (DSSCs) are low-cost devices that combine electroactive narrow bandgap organic molecules and wide bandgap inorganic semiconductors to produce a class of easily fabricated photovoltaics that exhibit high power efficiencies. Typical DSSCs comprise a photosensitizing dye adsorbed onto an inorganic semiconductor, such as TiO<sub>2</sub> or ZnO, which serves as the photoanode;<sup>3,4</sup> an electrolyte containing the I<sup>−</sup><sub>3</sub>/I<sup>−</sup> redox pair; and a catalytically active counter electrode (CE). The CE is an essential component of DSSCs, because it sustains the recombination of oxidized dyes and eliminates the concentration potential in the internal circuit,<sup>5</sup> therefore, leading to an enhancement of photoconversion efficiency. Platinum (Pt) is the traditional material used for catalyzing the redox pairs at the CE of DSSCs because of its high conductivity and excellent electrocatalytic activity.<sup>6</sup> However, the high cost of Pt limits its application in large-scale manufacturing and long-term operation.<sup>7</sup>

Recently, a large number of conductive polymers, such as polyaniline, polypyrrole, and poly(3,4-ethylenedioxythiophene) (PEDOT),<sup>8–10</sup> and inorganic compounds, including sulfides, nitrides, and carbides,<sup>11–13</sup> have been successfully employed to replace Pt as CEs in DSSCs; however, the stabilities and catalytic activities of these substitutes are unsatisfactory.<sup>14</sup> As an important class of metallic particles, copper (Cu) nanostructures have captured the attention of researchers in the electronics industry and are expected to be an essential component in future nano-electronic devices, due to their distinctive electrical and thermal conductivities, excellent optical transparency, mechanical flexibility, and relatively low cost.<sup>15</sup> Moreover, Cu nanostructures, as an ideal CE, should possess high electrocatalytic activity for the reduction of triiodide contained in the electrolyte. Despite

several advantages, CEs based on Cu nanostructures still suffer from multiple problems, such as long-term chemical stability under catalytic reaction conditions. Cu nanostructures are easily oxidized to Cu<sub>2</sub>O or CuO in either air or the presence of trace molecular oxygen, leading to a significant increase in the sheet resistance of nanostructure composite films.<sup>16</sup> Therefore, it is necessary to suppress the oxidation of Cu nanostructures by introducing suitable materials to enhance the long-term chemical stability of the composite.

Reduced graphene oxide (rGO), a flat monolayer of sp<sup>2</sup>-bonded carbon atoms tightly packed into a two-dimensional honeycomb lattice, has attracted tremendous attention because of its properties, such as excellent charge carrier mobility at room temperature (200 000 cm<sup>2</sup> V<sup>−1</sup> s<sup>−1</sup>), superior electrical conductivity, and high surface area.<sup>17–19</sup> Although the chemical stability and catalytic activity of rGO is inadequate,<sup>14</sup> the formation of Cu nanostructures can largely improve the catalytic activity of the rGO-Cu composite. Modification of the counter electrode by rGO leads to an improvement in the conversion efficiency of DSSCs because the high conductivity of rGO promotes the electron transfer rate of the CE; delocalized electrons in rGO can move freely in the low resistance carbon network. Moreover, vacancies and dangling bonds in rGO can influence the electronic structure of adsorbed Cu atoms and improve their chemical stability.<sup>16</sup> Therefore, rGO acts as a protective layer to prevent the oxidation of Cu nanostructures. However, the aggregation of rGO during the reduction process dramatically decreases the surface area, which leads to a significant reduction in conductivity. To overcome this challenge, electrodeposition is used to prepare a thin film of rGO on the surface of the conductive electrode. Electrodeposition produces films of a controllable thickness that demonstrate a relatively high stability, due to parameters such as electrolyte concentration, current density, scan rate, etc.

Building on these ideas, we reported an electrochemical route for the fabrication of an organic-metal layer-by-layer structured CE that was exemplified by an rGO-Cu hybrid. The facile electrodeposition process allows for precise control over multiple deposited layers, without the need for organic binders and additives. Moreover, the rGO-Cu composite has the potential to replace Pt as a low-cost CE in DSSCs that consists of a photoanode based on an array of ZnO nanorods. Under visible light irradiation, current density–voltage curves and photocurrent properties were obtained to gain insight into the effect of rGO loading in an rGO-Cu CE, which was matched with a ZnO nanorod photoanode in a DSSC.

<sup>z</sup>E-mail: m.sookhakian@gmail.com; erfana@hanyang.ac.kr; yatimah70@um.edu.my

## Experimental

**Chemical reagents.**—All chemicals, which were purchased from Merck Co., were of analytical purity and used without further purification. Double distilled water was utilized for all experimental procedures. All experiments were performed at atmospheric air pressure.

**Electrodeposition of rGO and layer-by-layer electrodeposition of rGO-Cu CE.**—Micron-sized graphite powder (1–2  $\mu\text{m}$ , Sigma Aldrich) was utilized as a precursor for the synthesis of graphene oxide (GO) by a modified Hummers' method.<sup>20</sup> The electrodeposition of rGO films with different rGO loadings used a three-electrode electrochemical cell and was carried out by a single voltammetric cycle. A clean ITO-coated glass substrate was used as the working electrode, while a platinum wire served as the counter electrode. The solutions contained 15 ml of different concentrations of GO (0.1  $\text{mg ml}^{-1}$ , 0.5  $\text{mg ml}^{-1}$ , and 1  $\text{mg ml}^{-1}$ ) and 5 ml of 0.025 M  $\text{Mg}(\text{NO}_3)_2$ . The applied potential, with respect to an Ag/AgCl reference electrode, ranged from 0.0 to  $-1.5$  V at a  $2 \text{ mV s}^{-1}$  scan rate.

Fresh rGO-modified ITO thin film electrodes with different rGO loadings were then utilized as working electrodes for the Cu nanopolyhedra growth by cyclic voltammetry in five cycles with respect to an Ag/AgCl reference electrode, while a platinum wire served as the counter electrode. The solution contained 20 ml of a 0.25 M  $\text{CuSO}_4$  and 0.3 M  $\text{H}_3\text{BO}_3$  solution. The applied potential ranged from  $-0.2$  to  $-1.5$  V at a  $50 \text{ mV s}^{-1}$  scan rate. The modified CEs with rGO loadings of 0.1  $\text{mg ml}^{-1}$ , 0.5  $\text{mg ml}^{-1}$ , and 1  $\text{mg ml}^{-1}$  were called rCu-1, rCu-2, and rCu-3, respectively. Pure Cu-modified ITO electrode was prepared using the same procedure but with the absence of the rGO.

**Electrodeposition of the ZnO nanorod array photoanode.**—The electrodeposition of ZnO nanorod arrays on an ITO electrode surface was performed as detailed in our previous work.<sup>21</sup> Briefly, the electrodeposition of ZnO nanorod arrays employed a three-electrode electrochemical cell immersed in a water bath that was maintained at  $70^\circ\text{C}$ . The fresh ITO electrode was used as the working electrode for the nanostructure growth by chrono-amperometry at  $-1.1$  V with respect to an Ag/AgCl reference electrode, while a platinum wire served as the counter electrode. The solution contained 0.001 M  $\text{Zn}(\text{NO}_3)_2$ , and a 0.1 M KCl solution served as the supporting electrolyte to increase conductivity. The deposition time was 90 min.

**Device fabrication and photoelectrochemical measurements.**—The ZnO-modified ITO film was soaked overnight in a ditetrabutylammonium cis-bis(isothiocyanato)bis(2,2'-bipyridyl-4,4'-dicarboxylato)ruthenium(II) (used as-received from Sigma Aldrich) solution (0.3 mM in ethanol). The DSSCs were assembled by combining a working electrode, which consisted of ITO modified by a ZnO nanorod array, an rCu- $x$  ( $x = 1, 2$ , and 3) film as the CE, and an electrolyte-filled  $50 \mu\text{m}$  thick spacer. The  $\text{I}_3^-/\text{I}^-$  liquid electrolyte consisted of 0.5 M KI, 0.05 M  $\text{I}_2$ , 0.6 M tetrabutylammonium iodide, and 0.5 M 4-tert-butylpyridine in acetonitrile. An active area of  $0.5 \text{ cm}^2$  was used to measure the cell performance. A PLS-SXE150 halogen lamp (Beijing Perfectlight Technology Corp., China) was utilized as an illumination source. The light intensity at the photoanode was  $20 \text{ mW/cm}^2$ , and the distance between the working electrode and the lamp was approximately 40 cm. The photocurrent was recorded continuously during both on and off periods. Transient photocurrent measurements and electrochemical impedance spectroscopy (EIS) measurements were performed using a potentiostat/galvanostat (Autolab PGSTAT30) from Ecochemie (Netherlands).

**Characterization.**—The phase and crystallite size of the samples were characterized using an automated X-ray powder diffractometer (XRD, PANalytical's Empyrean) equipped with a monochromated Cu  $K\alpha$  radiation source ( $k = 1.54056 \text{ \AA}$ ). The particle size and structural characterization of the as-synthesized product were determined using high-resolution field-emission scanning electron microscopy

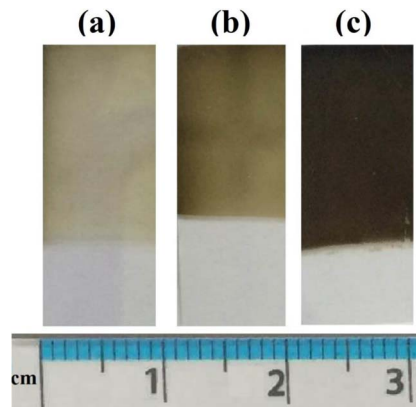


**Figure 1.** Photo of rGO-modified ITO electrodes with different concentrations of rGO: (a) 0.1  $\text{mg ml}^{-1}$ , (b) 0.5  $\text{mg ml}^{-1}$ , and (c) 1  $\text{mg ml}^{-1}$ .

(FESEM-Hitachi SU8000). Fourier transform infrared (FTIR) analysis was performed on a Perkin Elmer System 2000 series spectrophotometer (USA) between  $4000$  and  $600 \text{ cm}^{-1}$ . Raman spectroscopy was performed using a Renishaw InVia Raman Microscope with laser excitation ( $k = 514 \text{ nm}$ ).

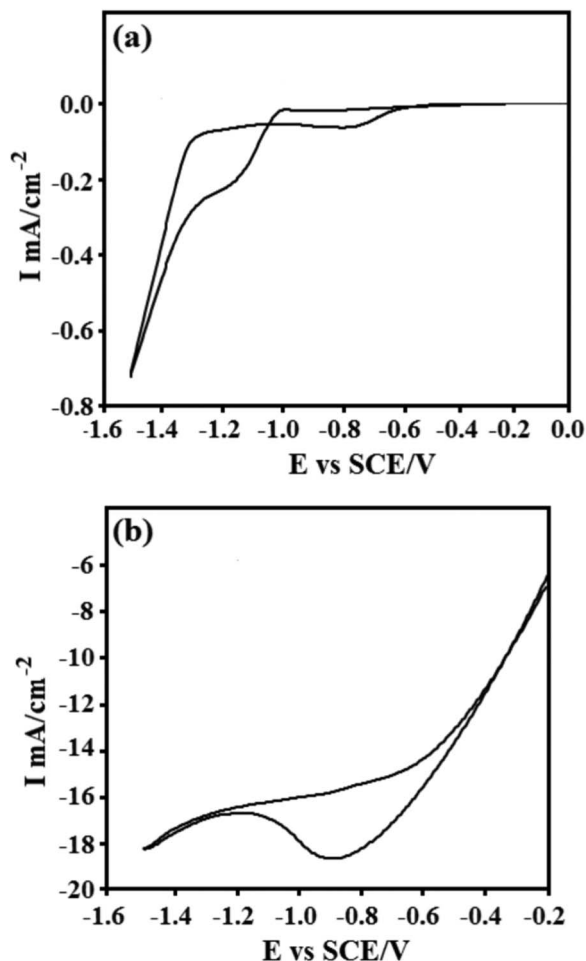
## Results and Discussion

**Characterization of rGO-Cu-modified ITO CE.**—The uniform electrodeposition of rGO-modified ITO thin film electrodes reveals that an increase in rGO loading results in a brown color, which is due to an increase in the thickness of the rGO film (Fig. 1). The cyclic voltammograms (CVs) of the rGO-modified ITO electrode with a 0.5  $\text{mg ml}^{-1}$  concentration of GO is illustrated in Fig. 2a. Two reduction peaks are observed in the negative scan of the graph, which shows the successful reduction of GO. The first peak at  $-0.8$  V may be attributed to the reduction of oxygen-containing groups on the graphene plane that are too stable to be reduced by cyclic voltammetry.<sup>22</sup> The second cathodic peak, which starts at ca  $-1.3$  V, corresponds to the irreversible electrochemical reduction of GO.<sup>22</sup>

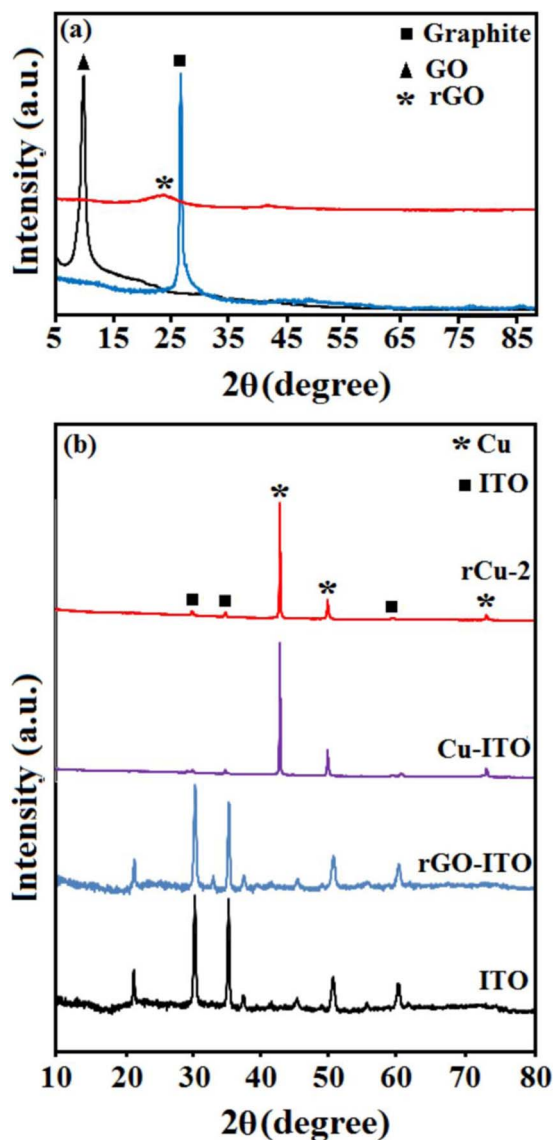
Fig. 2b shows the CV profiles for the electrodeposition of Cu nanopolyhedra on the surfaces of rGO-modified ITO electrodes in a potential range from  $-0.2$  to  $-1.5$  V. The cathodic current peak starts to increase at a potential of  $-0.2$  V and reaches a maximum of  $-18.5$  mA at approximately  $-0.85$  V, which is attributed to the reduction of  $\text{Cu}^{2+}$  to form metallic Cu.<sup>23</sup> At potentials higher than  $-0.85$  V, the current decreases to  $-16.5$  mA and is accompanied by a minor plateau, which is attributed to a mass-transport controlled process. The plateau may be associated with a depletion of copper species at the interface of the working electrode and indicates a nucleation and growth mechanism that is controlled by diffusion.<sup>23</sup> Further scanning leads to an increase in the current that may be attributed to a secondary reaction involving hydrogen evolution.

Fig. 3a shows the X-ray diffractograms of graphite, GO, and rGO. An intense, sharp diffraction peak for GO appears at  $2\theta = 10.6^\circ$ , which is assigned to the (001) lattice plane and corresponds to a d-spacing of  $0.83 \text{ nm}$ . This d-spacing is much wider than that of the narrow graphite peak located at  $26.8^\circ$ , which has an interlayer spacing of  $0.33 \text{ nm}$ . This result indicates that GO sheets have been effectively exfoliated from the raw graphite.<sup>24</sup> As a basis for comparison, the 5-cycle electrodeposition of rGO, which was subsequently separated from the ITO, gives a diffractogram where the strong GO peak is replaced by a very broad (002) peak at a  $2\theta$  of  $24.28^\circ$ . This corresponds to an interlayer spacing of  $0.36 \text{ nm}$  and indicates that GO was reduced to rGO sheets during the electrodeposition process.

The phase structure of the layer-by-layer electrodeposited rCu-2-modified ITO electrode is illustrated in Fig. 3b. It is clear that the rGO-modified ITO electrode exhibits a similar XRD pattern to the blank ITO electrode, i.e., the absence of diffraction peaks that are



**Figure 2.** (a) The CV profile of an as-electrodeposited rGO ( $0.5 \text{ mg ml}^{-1}$ )-modified ITO electrode, and (b) the CV profile of an as-electrodeposited Cu.



**Figure 3.** (a) XRD patterns of graphite, GO and rGO; (b) XRD patterns of bare ITO, rGO-ITO and rCu-2 CE.

typical of rGO, which may be due to the limited amount of rGO in the sample.<sup>21</sup> However, the Cu-modified ITO electrode does generate diffraction peaks at  $2\theta$  values of  $43.298^\circ$ ,  $50.434^\circ$ , and  $74.133^\circ$ , which can be indexed to the (111), (200), and (220) lattice planes of cubic copper (JCPDS card no. 00-004-0836), respectively, with the lattice constant  $a = b = c = 3.615 \text{ \AA}$ . It is apparent that the rCu-2 electrode exhibits similar XRD patterns with blank Cu-modified ITO electrode i.e., the existence of rGO does not affect the growth of new crystal orientations of Cu; thus, rGO only functions as a platform where the Cu nanopolyhedra can nucleate and grow.

The efficient reduction of GO to rGO after the electrodeposition is verified by FTIR and Raman spectroscopies (Figs. 4–5). The FTIR spectrum of pristine GO shows all of the characteristic bands for GO: the broad peak centered at  $3329 \text{ cm}^{-1}$  is assigned to the OH stretching vibration, the C = O stretching vibration is at  $1739 \text{ cm}^{-1}$ , the stretching vibration of  $\text{sp}^2$  hybridized C = C is at  $1635 \text{ cm}^{-1}$ , the OH bending vibration of C-OH is at  $1405 \text{ cm}^{-1}$ , the C-OH stretch is at  $1172 \text{ cm}^{-1}$ , and the C-O stretching vibration is at  $1047 \text{ cm}^{-1}$ ; and the absorption peak at approximately  $584 \text{ cm}^{-1}$  is due to epoxide groups that are situated at the edge of the GO sheet<sup>24</sup> (Fig. 4). In contrast, the FTIR spectrum of the rGO indicates that GO was reduced during the electrodeposition, as evidenced by the removal of certain peaks. The peaks that are associated with epoxide groups at the edge and C-OH at  $584 \text{ cm}^{-1}$  and  $1172 \text{ cm}^{-1}$  are absent, while the noticeable decrease in the intensities of the peaks at  $1047$  and  $1405 \text{ cm}^{-1}$  implies that a large fraction of the oxygen and OH groups were removed.

Raman spectroscopy is a powerful technique for investigating the structural and electronic properties of carbon compounds. Fig. 5

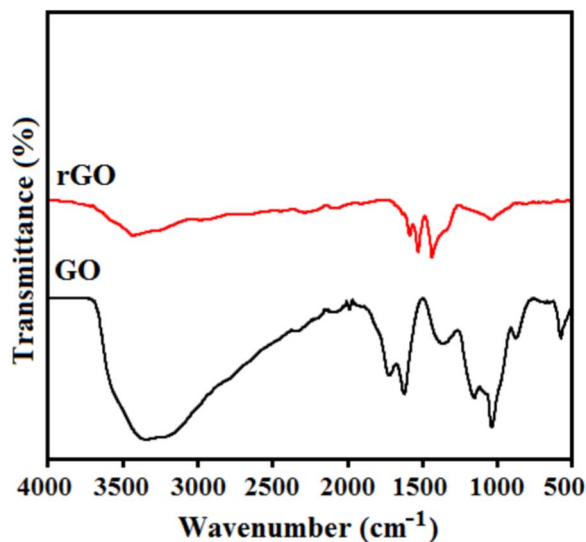


**Figure 4.** The FTIR spectra of GO and as-electrodeposited rGO.



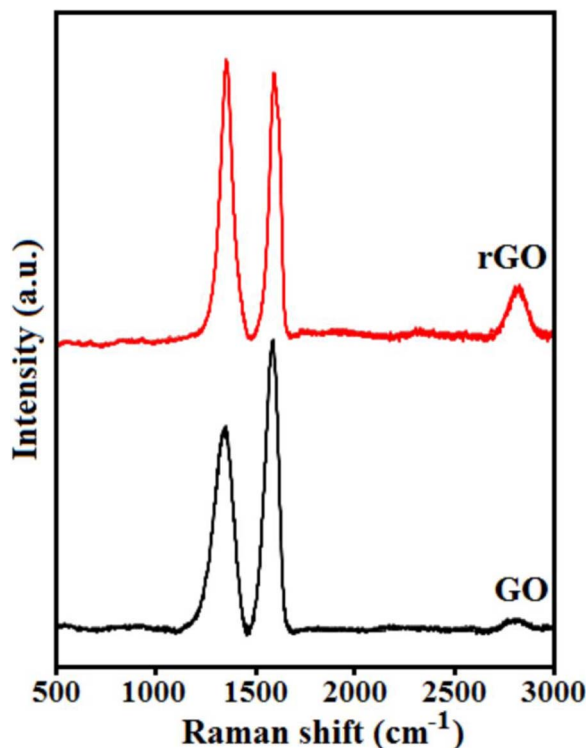


**Figure 5.** The Raman spectra of GO and as-electrodeposited rGO.

compares the Raman spectra of GO and the rGO-modified ITO electrode. The Raman spectrum of the GO-modified ITO electrode shows three peaks at 1359, 1588 and 2688  $\text{cm}^{-1}$ , which correspond to the D, G and 2D bands, respectively. The G band arises from the in-plane bond stretching of the carbon  $\text{sp}^2$  bond, whereas the D band is associated with various types of defects, such as vacancy-like defects and  $\text{sp}^3$  defects that can be produced by oxidation and hydrogenation, grain boundary edges, domain boundaries and electron doping.<sup>25,26</sup> Furthermore, the intensity of the 2D band (activated by a two-phonon double-resonant Raman process) is reciprocal to the electron-hole scattering rate.<sup>25</sup> With the reduction of GO, the D and G bands shifted to 1347 and 1584  $\text{cm}^{-1}$ , respectively, which are lower than the corresponding GO bands. Furthermore, the intensity of the 2D peak at approximately 2683  $\text{cm}^{-1}$  increased, which indicates a greater number of electrodeposited rGO, when compared with GO.<sup>24</sup> The intensity ratio of the D to G bands ( $I_D/I_G$ ) for GO and the rGO-modified ITO electrode are 0.66 and 1.08, respectively. The increase in  $I_D/I_G$  implies that the electrodeposition generates a considerable amount of  $\text{sp}^2$  bonds and structural defects in the rGO lattice.<sup>24</sup>

FESEM was utilized to study the morphology of the rGO- and rGO-Cu-modified ITO electrodes (Fig. 6). The top view image of an rGO-modified ITO electrode (Fig. 6a) before the deposition of Cu nanopolyhedra shows a surface that is flat with typical wrinkle-like features that are slightly visible. The low magnification FESEM image of the as-electrodeposited rCu-2-modified ITO electrode (Fig. 6b) clearly shows that the Cu formed as polyhedral nanostructures and are uniformly and densely distributed on the surface, i.e., no areas of the graphene sheets without Cu nanopolyhedra decoration are found. Zoomed-in views (Figs. 6c–6d) reveal that the individual Cu nanopolyhedra possess sizes in the range of 80–100 nm. Moreover, with the increased rGO loading no significant changes in the particle sizes of Cu nanopolyhedra have been observed (Figs. S1a and b). In addition, the rGO nanosheets can function as conductive links between the various Cu nanopolyhedra. This facilitates the transfer of photo-generated charge carriers and enhances the photovoltaic performance and transient photocurrent of the DSSCs.

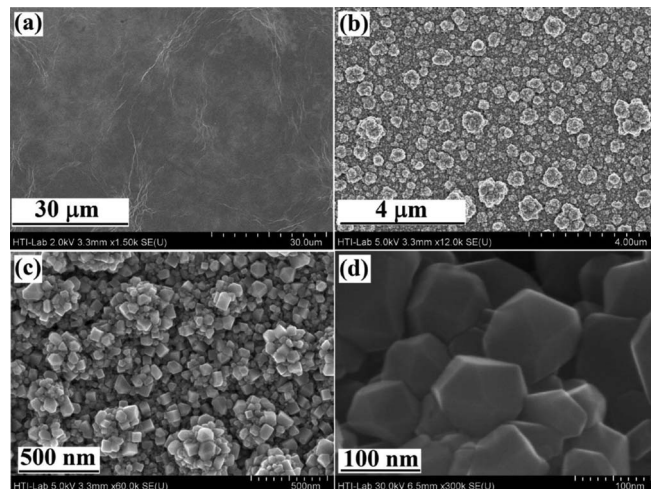


**Figure 6.** (a) An FESEM image of as-electrodeposited rGO nanosheets on an ITO substrate; (b) a top view FESEM image of the rCu-2-modified ITO CE; and (c–d) low and high magnification FESEM images of the rCu-2-modified ITO CE.

**Photoelectrochemical performance.**—A schematic of the DSSC device fabricated with the layer-by-layer electrodeposited rGO-Cu-modified ITO electrode as the CE is shown in Fig. 7. To investigate the influence of rGO and copper CEs on the photoelectrochemical conversion efficiency of the DSSCs, current density–voltage ( $J$ – $V$ ) measurements of devices fabricated with an electrodeposited ZnO nanorod photoanode and with different CEs were performed under 100  $\text{mW cm}^{-2}$  light illumination at room temperature (Fig. 8); the different CEs include rCu-1-, rCu-2-, and rCu-3-modified ITO electrodes, as well as an ITO electrode modified with copper nanopolyhedra. Table I summarizes the open-circuit voltage ( $V_{OC}$ ), short-circuit photocurrent density ( $J_{sc}$ ), fill factor (FF), and power conversion efficiency ( $\eta$ ) for each of the cells.

As observed in Fig. 8, the presence of rGO in the CE based pure Cu nanopolyhedra leads to an enhancement in the conversion efficiency from 3.34% to 5.03%. For an increase in rGO loading up to 0.5  $\text{mg ml}^{-1}$ , the  $J_{sc}$  increases from 12.68  $\text{mA cm}^{-2}$  for rCu-1 to 13.01  $\text{mA cm}^{-2}$  for rCu-2; however, further increasing the rGO loading up to 1  $\text{mg ml}^{-1}$  leads to a decrease in  $J_{sc}$ . Therefore, the optimized conver-

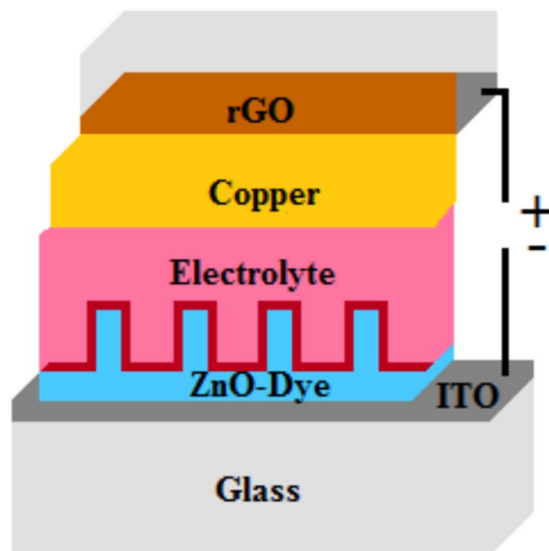


**Figure 7.** A schematic representation of the solar cell based on the ZnO nanorod array as a photoanode and the rCu-2-modified ITO electrode as a CE.

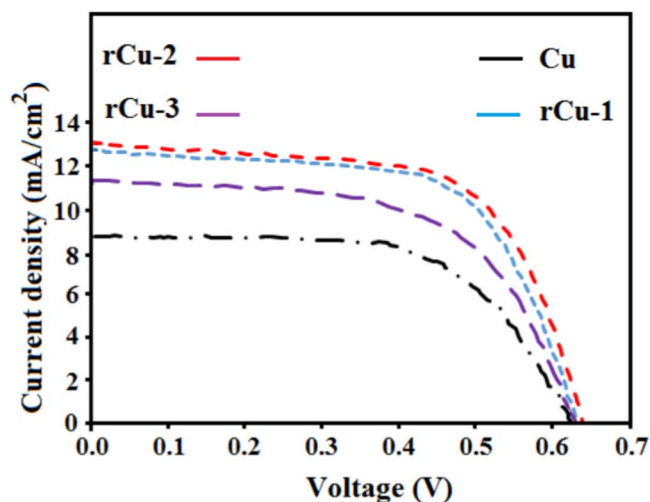


**Figure 8.** J-V curves of DSSCs based on pure Cu and rCu-*x* (*x* = 1, 2 and 3) CEs.

**Table I.** Photovoltaic parameters of the DSSCs based on different CEs.

Sample	$V_{oc}$ (V)	$J_{sc}$ (mAcm <sup>-2</sup> )	FF	$\eta$ (%)
Cu	0.62	9.14	0.59	3.34
rCu-1	0.63	12.68	0.63	5.03
rCu-2	0.65	13.01	0.64	5.44
rCu-3	0.62	11.10	0.58	3.99

sion efficiency is obtained with the rCu-2 CE, with  $\eta = 5.44\%$  under AM 1.5 illumination ( $100 \text{ mW cm}^{-2}$ ), which is ca. 1.5-fold higher than  $\eta$  acquired with the pure Cu CE.

The measurement of the photocurrent transient response was performed under visible light irradiation to determine the influence of rGO loading on the photo-electrochemical properties of the DSSCs. The transient photocurrents of cells containing the different CEs are shown in Fig. 9. The applied bias was 0 vs. an SCE reference electrode. An anodic photocurrent of  $3.8 \text{ mA cm}^{-2}$  was obtained with the pure Cu CE when the light source was switched on, suggesting that the Cu nanopolyhedra may serve as a substitute for Pt (Fig. 9). Moreover, the dark current was negligible when the light source was switched off. When compared with the Cu nanopolyhedra CE, the presence of rGO

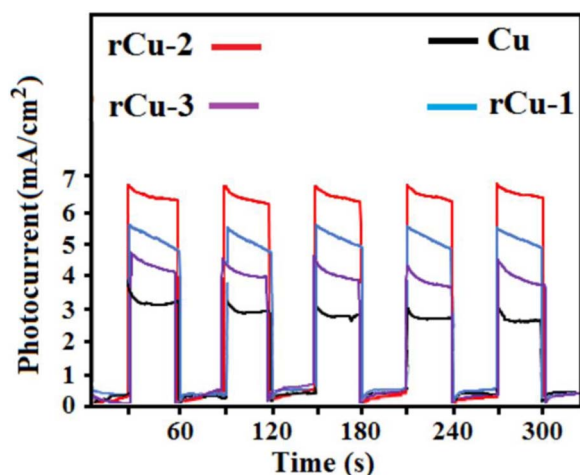


**Figure 9.** Photocurrent versus time (I-t) curves of DSSCs based on pure Cu and rCu-*x* (*x* = 1, 2 and 3) CEs.

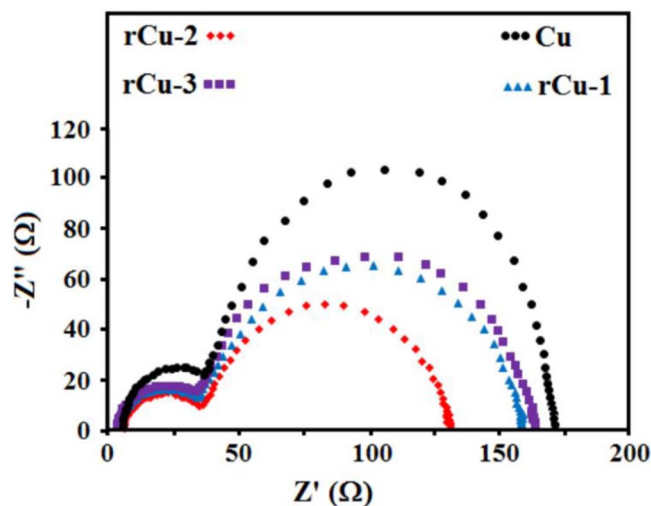


**Figure 10.** EIS Nyquist plots of DSSCs based on pure Cu and rCu-*x* (*x* = 1, 2 and 3) CEs.

leads to an enhancement of the transient photocurrent response from  $3.8 \text{ mA cm}^{-2}$  to  $5.8 \text{ mA cm}^{-2}$  for rCu-1. Further increasing the rGO loading up to  $0.5 \text{ mg ml}^{-1}$  results in a transient photocurrent of  $6.4 \text{ mA cm}^{-2}$  for rCu-2. However, an rGO loading of  $1 \text{ mg ml}^{-1}$  (rCu-3) leads to a decrease in the transient photocurrent down to  $4.9 \text{ mA cm}^{-2}$ . Thus, the optimized value is obtained from rCu-2 and represents an approximately 1.5-fold higher current than that exhibited by the Cu nanopolyhedra CE. Moreover, the transient photocurrents were rapid, steady, prompt and reproducible over several on-off illumination cycles for all CEs.

Based on the current density-voltage curves and the photocurrent transient response measurements, it is clear that rGO plays an important role in the catalytic activity of CEs, which enhances the power conversion efficiency and photocurrent response of the DSSCs. Therefore, electrochemical impedance spectroscopy (EIS) was performed under illumination by applying a 10 mV AC signal over a frequency range of  $1-10^5 \text{ Hz}$ , to evaluate the electrocatalytic activity of the counter electrode (Fig. 10). The EIS Nyquist plots of the DSSCs reveal a high-frequency response that is due to the

electrode-electrolyte interface, which is related to the reduction of  $\text{I}_3^-$  to  $\text{I}^-$  at the CE interface. The intermediate frequency response is associated with the charge transfer and recombination at the ZnO photoanode interface. Finally, the low-frequency response is ascribed to the Warburg diffusion process of  $\text{I}_3^-/\text{I}^-$  in the electrolyte medium. The semicircle with a larger diameter represents a larger interfacial resistance and a higher interfacial charge recombination at the interfaces.<sup>21</sup> Compared with the pure Cu-modified ITO CE, the presence of rGO leads to a significant decrease in the diameter of the high-frequency semicircle, which is evidence that the increased CE conductivity is due to the presence of rGO films. This increased conductivity apparently enhances the catalytic abilities of the CE, which results in an improved DSSC conversion efficiency. However, the diameter of the semicircle increased when the rGO content was raised above the optimum value ( $0.5 \text{ mg ml}^{-1}$ ), which illustrates a reduction in CE catalytic activity. This phenomenon is likely associated with a decreased CE conductivity resulting from excessive rGO content that leads to more agglomeration during the electrodeposition, which dramatically decreases the surface area<sup>27</sup> and significantly reduces the power conversion efficiency of the DSSC.

## Conclusions

rGO Nanosheets and 80–100 nm Cu nanopolyhedra were grown on an ITO substrate by a layer-by-layer electrochemical deposition. The FTIR and Raman results clearly show the conversion of graphene

oxide to reduced graphene oxide during the electrochemical deposition. rGO-Cu Hybrids with different rGO loadings were used as counter electrodes for DSSCs that are based on ZnO nanorod photoanodes. The current density-voltage curves demonstrated that the power conversion efficiencies of DSSCs as a function of the rGO loading, and a maximum conversion efficiency of 5.44% was at an rGO loading of  $0.5 \text{ mg ml}^{-1}$ . The EIS measurement proved that an increase in rGO loading up to  $1 \text{ mg ml}^{-1}$  leads to a rise in the electrolyte-electrode interfacial resistance and a reduced CE conductivity, which lowers the CE electrocatalytic activity and the power conversion efficiency of the DSSC.

### Acknowledgments

This research is supported by a High Impact Research MoE grant UM.C/625/1/HIR/MoE/SC/04 from the Ministry of Education Malaysia, UMRG Program RP012A-14SUS and the University Malaya Centre for Ionic Liquids (UMCiL). The work was also supported by the National Research Foundation of Korea (NRF) Grant (No. 2014M3A6B3063711), funded by the Korean Ministry of Education, Science and Technology (MEST).

### References

1. M. Sookhakian, Y. Amin, S. Baradaran, M. Tajabadi, A. M. Golsheikh, and W. Basirun, *Thin Solid Films*, **552**, 204 (2014).
2. S. H. Ko, *SmartSci.*, **2**, 54 (2014).
3. S. H. Ko, D. Lee, H. W. Kang, K. H. Nam, J. Y. Yeo, S. J. Hong, C. P. Grigoropoulos, and H. J. Sung, *Nano lett.*, **11**, 666 (2011).
4. I. Herman, J. Yeo, S. Hong, D. Lee, K. H. Nam, J.-h. Choi, W.-h. Hong, D. Lee, C. P. Grigoropoulos, and S. H. Ko, *Nanotechnology*, **23**, 194005 (2012).
5. Z. Gao, L. Wang, X. Liu, P. Guo, W. Zhao, D. Wu, F. Xu, and K. Jiang, *RSC Adv.*, **5**, 32096 (2015).
6. P.-T. Shih, R.-X. Dong, S.-Y. Shen, R. Vittal, J.-J. Lin, and K.-C. Ho, *J. Mat. Chem. A*, **2**, 8742 (2014).
7. S. Felix, B. P. Chakkravarthy, S. K. Jeong, and A. N. Grace, *J. Electrochem. Soc.*, **162**, H392 (2015).
8. S. Peng, L. Tian, J. Liang, S. G. Mhaisalkar, and S. Ramakrishna, *ACS appl. mater. interfaces*, **4**, 397 (2012).
9. Q. Tai, B. Chen, F. Guo, S. Xu, H. Hu, B. Sebo, and X. Z. Zhao, *ACS Nano*, **5**, 3795 (2011).
10. J. G. Chen, H. Y. Wei, and K. C. Ho, *Sol. Energy Mater. Sol. Cells*, **91**, 1472 (2007).
11. X. Xin, M. He, W. Han, J. Jung, and Z. Lin, *Angew. Chem.- Int. Edit.*, **50**, 11739 (2011).
12. Q. W. Jiang, G. R. Li, and X. P. Gao, *Chem. Commun.*, 7603 (2009).
13. M. Wu, X. Lin, A. Hagfeldt, and T. Ma, *Angew. Chem.- Int. Edit.*, **50**, 3520 (2011).
14. F. Gong, H. Wang, X. Xu, G. Zhou, and Z.-S. Wang, *J. Am. Chem. Soc.*, **134**, 10953 (2012).
15. C. Mattevi, H. Kim, and M. Chhowalla, *J. Mater. Chem.*, **21**, 3324 (2011).
16. X. Guo, C. Hao, G. Jin, H. Y. Zhu, and X. Y. Guo, *Angew. Chem.*, **126**, 2004 (2014).
17. M. Azarang, A. Shuhaimi, R. Yousefi, A. M. Golsheikh, and M. Sookhakian, *Ceram. Int.*, **40**, 10217 (2014).
18. M. Mahmoudian, Y. Alias, W. Basirun, P. M. Woi, and M. Sookhakian, *Sens. Actuator B-Chem.*, **201**, 526 (2014).
19. C. Schütter, C. Ramirez-Castro, M. Oljaca, S. Passerini, M. Winter, and A. Balducci, *J. Electrochem. Soc.*, **162**, A44 (2015).
20. M. Azarang, A. Shuhaimi, R. Yousefi, and M. Sookhakian, *J. Appl. Phys.*, **116**, 084307 (2014).
21. M. Sookhakian, Y. M. Amin, R. Zakaria, S. Baradaran, M. R. Mahmoudian, M. Rezayi, M. T. Tajabadi, and W. J. Basirun, *Ind. Eng. Chem. Res.*, **53**, 14301 (2014).
22. M. R. Mahmoudian, Y. Alias, and W. J. Basirun, *Electrochim. Acta*, **72**, 53 (2012).
23. C. Meudre, L. Ricq, J.-Y. Hihn, V. Moutarlier, A. Monnin, and O. Heintz, *Surf. Coat. Technol.*, **252**, 93 (2014).
24. M. Sookhakian, Y. Amin, R. Zakaria, W. Basirun, M. Mahmoudian, B. Nasiri-Tabrizi, S. Baradaran, and M. Azarang, *J. Alloy. Compd.*, **632**, 201 (2015).
25. M. Tajabadi, W. Basirun, F. Lorestani, R. Zakaria, S. Baradaran, Y. Amin, M. Mahmoudian, M. Rezayi, and M. Sookhakian, *Electrochim. Acta*, **151**, 126 (2015).
26. V. D. Dao, L. L. Larina, J. K. Lee, K. D. Jung, B. T. Huy, and H. S. Choi, *Carbon*, **81**, 710 (2015).
27. M. Azarang, A. Shuhaimi, and M. Sookhakian, *RSC Adv.*, **5**, 53117 (2015).